Sea Ice Meltwater in the Beaufort Gyre: A Comprehensive Analysis Using Sea Surface Salinity Data from SMOS

Eva De Andrés[1,2], Marta Umbert[2], María Sánchez-Urrea[2], Verónica González-Gambau[2], Estrella Olmedo[2], Carolina Gabarró[2], and Pedro Elosegui[2]

[1]Department of Applied Mathematics, Universidad Politécnica de Madrid, ETSIT-UPM, Madrid, Spain
[2]Barcelona Expert Center, Institute of Marine Sciences, ICM-CSIC, Barcelona, Spain

Key Points:

- SMOS sea surface salinity is a key tool for detecting freshening events induced by sea ice meltwater.
- Sea ice cover and sea surface salinity are tightly coupled and positively correlated.
- The ocean imprint (∼19 psu) of sea ice melt events that persist for up to 10 days are detected.

Corresponding author: Eva De Andrés, `eva.deandres@upm.es`

Abstract

Arctic sea ice is retreating, thinning, and exhibiting increased mobility. In the Beaufort Gyre (BG), liquid freshwater content (FWC) has increased by 40% in the last two decades, with sea ice melting being a primary contributor. This study utilizes satellite observations of sea surface salinity (SSS) and sea ice concentration, along with model-based sea ice thickness from 2011 to 2019. The aim is to investigate the sea ice-SSS relationship at different scales in the Arctic and understand the sea-ice meltwater dynamics in the BG. Our findings reveal a strong synchrony and positive correlation between sea ice area and SSS in the Arctic Ocean. In September, when the BG exhibits the largest ice-free ocean surface, a noticeable release of freshwater from sea ice melting occurs, a phenomenon not accurately reproduced by the models. The SMOS (Soil Moisture and Ocean Salinity) mission proves valuable in detecting meltwater lenses (MWL) originating from sea ice melting. These MWLs exhibit mean SSS ranging from 19 psu at the begining of sea ice retreat to 25 psu before sea ice formation. Wind-driven anticyclonic eddies can trap MWLs, preserving the freshest SSS imprints on the sea surface for up to 10 days. Furthermore, events of sea surface salinification following sea ice formation suggest that SMOS SSS might be capturing information on brine rejection. The daily evolution of sea ice-SSS within the MWLs demonstrates a tight correlation between both variables after sea ice melting and just before sea ice formation, indicating a transient period in between.

Plain Language Summary

The Arctic sea ice is changing. It's becoming younger, thinner, and more mobile. In the Beaufort Gyre (BG), the amount of liquid freshwater has increased by 40% over the last two decades, mainly due to melting sea ice. This study, using satellite data and models, explores how sea ice and sea surface salinity (SSS) are connected in the Arctic. It focuses on the BG to understand how melting sea ice contributes to freshwater. Results show a strong link between the area covered by sea ice and SSS in the Arctic Ocean. In September, when the BG has the most open water, there's a noticeable release of freshwater from melting sea ice that is not accurately represented by the models. The SMOS mission is useful in detecting areas of melted ice (MWL) characterized by low salinity and temperature. These MWLs can be trapped by ocean currents, keeping the freshest patterns for up to 10 days. The data also hints at brine rejection events after sea ice forms. Daily changes in sea ice and SSS within MWLs show a clear connection after ice melts and just before it forms again, suggesting a transitional period in between.

1 Introduction

The Arctic has warmed nearly four times faster than the globe since 1979 (Rantanen et al., 2022), experiencing a reduction in sea ice extent, thinning of the ice cover, warming and freshening of the Arctic Ocean, increased mixing and enhanced interactions within the ocean-ice-atmosphere system (Solomon et al., 2021).

Arctic freshwater originates from sea ice melting, glacial runoff, Arctic rivers, and precipitation (snowfall and rainfall) (Timmermans & Toole, 2023). This freshwater is retained within the upper layer, situated above the halocline and the Atlantic layer. The halocline serves as a crucial barrier, segregating Atlantic water heat from the surface and overlying sea ice (Polyakov et al., 2017). In the Pacific sector of the Arctic, the halocline is primarily influenced by Pacific Waters, which is a significant source of both heat and freshwater for the Arctic Ocean (Shimada et al., 2005). This influx occurs through the Bering Strait, playing a key role in the summer retreat of sea ice, particularly in the Beaufort Gyre (BG) (Shimada et al., 2001; Zhang, Lindsay, et al., 2008; Zhang, Steele, & Woodgate, 2008).

The BG is a key driver of Arctic Ocean salinity changes, as it is the largest reservoir of liquid freshwater content (FWC) in the Arctic Ocean, storing an average of 21,800 km^3 of FWC between 2003 and 2018 (Proshutinsky et al., 2019). Climate studies have recently focused on the BG freshening due to its capacity to eventually release substantial volumes of freshwater into the Arctic Ocean (Haine et al., 2015; Carmack et al., 2016), which is known to increase with future climate change (Jahn & Laiho, 2020). The freshwater may be transported to the subpolar North Atlantic through eddies or gyre spin-down mechanisms, driving salinity and density decrease (Dickson et al., 1988; Belkin et al., 1998). As the subpolar North Atlantic is an important region for deep-water formation, such freshening could impact the strength of the Atlantic Meridional Overturning Circulation (AMOC)(Jahn & Holland, 2013; Yang et al., 2016; Wang, Wekerle, Danilov, Wang, & Jung, 2018; Holliday et al., 2020; Zhang et al., 2021; Haine et al., 2023) and have broader global effects (Rahmstorf et al., 2015).

Sustained by the anticyclonic winds of the climatological Beaufort Sea High (Serreze & Barrett, 2011; Timmermans & Marshall, 2020), the upper-ocean circulation within the BG drives Ekman convergence and deepening of the halocline (Proshutinsky et al., 2002). Observations of hydrographic data and satellite-derived sea surface height measurements have revealed a substantial freshening of the Beaufort Gyre since the mid-1990s (Proshutinsky et al., 2009; Rabe et al., 2011; Giles et al., 2012; Krishfield et al., 2014). Notably, there has been a 40% increase in FWC during 2003-2018 compared to the previous climatology (Proshutinsky et al., 2019). These changes have been attributed to a combination of an anticyclonic atmospheric circulation, increased surface anticyclonic stress resulting from retreated sea ice cover, direct contributions from sea ice melt, and wind-driven redirection of low salinity flows from the Mackenzie River (Proshutinsky et al., 2019; Giles et al., 2012; Wang, Wekerle, Danilov, Wang, & Jung, 2018; Armitage et al., 2020; Johnson et al., 2018).

Recent research has pointed out the important role that sea ice transport exerts in redistributing freshwater into and out of the BG (Cornish et al., 2023). The ocean surface freshening induced by sea ice melting has been shown to restrict the momentum transfer from the atmosphere to the ocean, thereby enhancing near-surface stratification of the upper ocean (Supply et al., 2022). However, the impact of sea ice retreat on freshwater dynamics and the broader climate system remains poorly constrained, being an active area of current scientific research.

Traditional estimation of the Arctic Ocean's FWC using in situ measurements faces challenges of limited spatiotemporal sampling and high costs. In recent decades satellite data, in situ observations, and model reanalysis outputs have been integrated not only for FWC estimations (e.g. Fournier et al. (2020); Solomon et al. (2021); Umbert et al. (2023)) but also for improved analysis of sea ice decline and river discharge impact on the Arctic Ocean (Kilic et al., 2018), as well as in detecting a punctual meltwater lens (MWL) induced by sea ice melting (Supply et al., 2022).

The Soil Moisture and Ocean Salinity (SMOS) is a satellite mission from the European Space Agency to measure the sea surface salinity (SSS) of the ocean. SMOS provides daily full coverage in polar regions, with an effective spatial resolution of $\sim$50 km in ice-free areas (Martínez et al., 2022). Despite lower sensitivity in polar oceans due to low sea surface temperatures (SST), recent advances in retrieval algorithms have led to tailored Arctic products (Martínez et al., 2022), facilitating the integration of SSS data into Arctic studies (e.g. Fournier et al. (2019); Hall et al. (2021); Umbert et al. (2021, 2023)).

Our study explores the relationship between sea ice cover and SSS across various scales in the Arctic and quantifies the volume of freshwater released from sea ice melting in the BG by integrating satellite data and reanalysis outputs. In addressing potential solutions for filling spatiotemporal gaps in satellite data, we assess and compare the

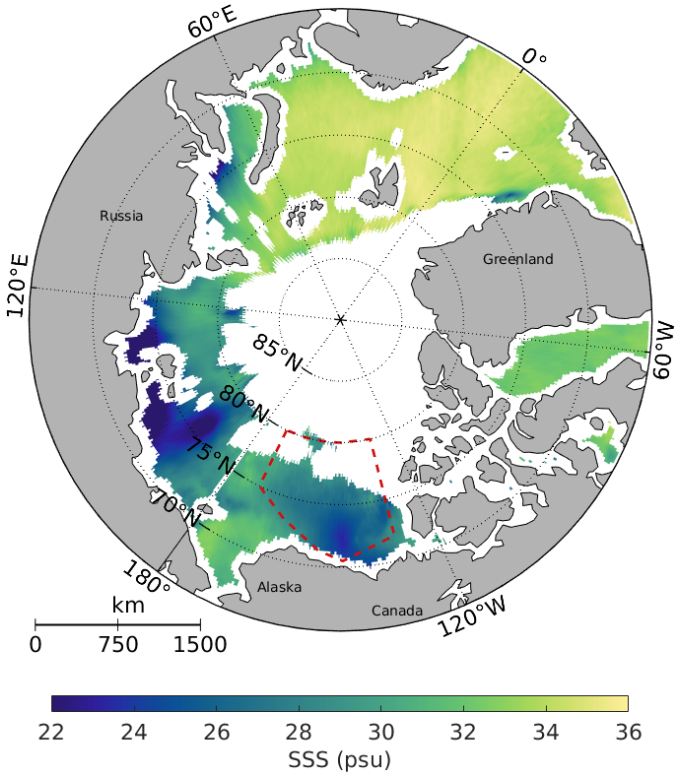

Figure 1: SMOS sea surface salinity over the Arctic ocean (>65°N) in September 2012. The Beaufort Gyre region is delimited by the dashed red polygon.

accuracy of two reanalysis SSS outputs in regions significantly impacted by sea ice melting against SMOS SSS. Leveraging the capabilities of SMOS SSS, we localize and monitor the extent of MWLs induced by sea ice melting every September from 2011 to 2019, compute the volume of freshwater released within these MWLs and characterize their SST-SSS and density imprints. The impact of distinct atmospheric regimes on the daily evolution of MWL properties is analyzed and discussed. To close our study, the sea ice-SSS relationship is revisited at the local MWL scale.

2 Data

Our study spans from 2011 to 2019. Different data sets from both remote sensors and reanalysis outputs are used and analyzed over the Arctic north of 65°N and the BG area proposed in Proshutinsky et al. (2019) (Fig.1). All the data used in this study refer to the sea surface level, meaning that they are spatially 2D variables, which do not include the vertical component. All data sets were spatially regridded onto the same regular latitude-longitude mesh grid of 0.25^{o} horizontal resolution.

2.1 Satellite observations: Sea Surface Salinity, Sea Ice Concentration and Sea Surface Temperature

We use the SMOS SSS v3.1 Arctic product from the Barcelona Expert Center (BEC) (Martínez et al., 2022), a specially tailored product for the Arctic Ocean with improved effective spatial resolution that permits better monitoring of the mesoscale structures larger than 50 km. The salinity maps used in this analysis are generated on a daily ba-

sis, using a 9-day running mean, in an Equal-Area Scalable Earth grid (EASE 2.0) (Brodzik et al., 2012)) of 25 km horizontal spatial resolution from 2011 to 2019. Note that SMOS only retrieves SSS within free-of-ice ocean areas.

The Ocean and Sea Ice Satellite Application Facility (OSISAF) from the European Organization for the Exploitation of Meteorological Satellites (EUMETSAT) provides sea ice concentration (SIC) data computed from atmospherically corrected SSMIS (Special Sensor Microwave Imager Sounder) brightness temperatures, using a combination of state-of-the-art algorithms. The product series has been operational since 2005. The SIC data used in this work is the version OSI-450 until 2016 (Lavergne et al., 2019; EUMETSAT Ocean and Sea Ice Satellite Application Facility, Darmstadt, Germany, 2017) and OSI-430-b from 2016 onwards (EUMETSAT Ocean and Sea Ice Satellite Application Facility, Darmstadt, Germany, 2019), which both provide daily-averaged fractional ice cover in percentage, on an EASE 2.0 grid of 25 km horizontal resolution over a Global Lambert azimuthal projection.

We use the satellite-derived dataset of daily SST from OSTIA (Operational Sea Surface Temperature and Sea Ice Analysis) at a horizontal resolution of 0.05 degrees, which translates to about 3 km at latitude 70°N (Good et al., 2020)). OSTIA uses satellite data provided by the GHRSST (Group for High Resolution Sea Surface Temperature) together with in situ observations to determine the sea surface temperature. OSTIA SST is obtained blending both infrared and microwave radiometers such as the Advanced Very High-Resolution Radiometer (AVHRR) on NOAA satellites and the Moderate Resolution Imaging Spectroradiometer (MODIS) on NASA's Aqua and Terra satellites.

2.2 Ocean Reanalysis: Sea Surface Salinity, Sea Ice Thickness, Wind Stress, and Sea Ice Velocity

ORAS5 (Ocean Reanalysis System 5) provides monthly mean global ocean and sea-ice reanalysis data from the ECMWF (European Centre for Medium-Range Weather Forecasts) OCEAN5 (ocean analysis-reanalysis system). OCEAN5 uses the NEMO (Nucleus for European Modelling of the Ocean) ocean model and assimilates sub-surface temperature and salinity, satellite sea-ice concentration, and sea-level anomalies. ORAS5 is forced by atmospheric reanalysis and constrained by observational data of SST, SSS, SIC, global-mean-sea-level trends, and climatological variations of the ocean mass. The ocean model is projected on a tripolar grid, and has an eddy-permitting horizontal resolution of 0.25^{o} and 75 vertical levels with near-surface resolution of 1 m. In this work, we used the consolidated (2011-2014) and operational (2015-2019) ORAS5 sea ice thickness (SIT), SST, wind stress, and sea ice velocity.

TOPAZ reanalysis product is released by the Arctic Monitoring and Forecasting Center of CMEMS (Copernicus Marine Service). The data sets of its latest version, TOPAZ4b, are used in this study. TOPAZ4b uses the Hybrid Coordinate Ocean Model (HYCOM) coupled to a sea ice model, which includes ice thermodynamics and elastic-viscous-plastic rheology. The TOPAZ4b native grid is built on a Polar stereographic North projection. It covers the Arctic and North Atlantic Oceans and has horizontal spatial resolution between 11 km at the North Pole and 16 km at the southernmost grid cells. It is composed of 40 hybrid (z-isopycnal) vertical levels, with resolution varying from 1 m at the surface to 1500 m at the deepest level. TOPAZ4b weekly assimilates observations, including along-track Sea Level (SL) anomalies from satellite altimeters, SST from OSTIA, in situ temperature and salinity from hydrographic cruises and moorings, OSISAF SIC, Cryosat-SMOS SIT and SMOS SSS v3.1 from BEC. TOPAZ4b provides yearly, monthly, and daily outputs at all depths. We used the monthly-averaged SSS in our study.

3 Methods

3.1 Computation of Sea Ice Area

To get a general view of how salinity at the ocean surface behaves under sea ice melting/formation, horizontally-averaged monthly means of SSS and SIC were calculated over both the Arctic and the BG (see both regions in Fig.1). From SIC, we computed the sea ice area (SIA), which is defined in Lavergne et al. (2023) as "the total ocean area covered by any amount of ice (no SIC threshold applied, and the SIC value weights the grid cell area)". Therefore,

$$SIA = \sum_{i=1}^{N} \alpha_i a_i, \tag{1}$$

where N is the number of grid cells inside the given region, α_i represents the grid-cell fraction covered by sea ice (SIC/100), and a_i is the grid-cell area, estimated with the Climate Data Toolbox for Matlab (Greene et al., 2019), assuming Equatorial and Polar radius of 6378.1 and 6356.8 km, respectively. Note that SIE (sea ice extent) is considered a more reliable index for monitoring sea ice evolution in time, however, we have focused on SIA, because it is the variable needed to ultimately compute the freshwater released from sea ice melting (see Eqn. 2). We then analyzed the time evolution of the SSS and SIA variables and evaluated their synchrony and relationship through correlation tests.

3.2 Evaluation of Reanalysis Performance

SSS monthly means of ORAS5 and TOPAZ4b were compared with monthly means of SMOS SSS to analyze the goodness of each reanalysis performance. Cell-to-cell differences between remotely sensed observations and model-based outputs of SSS data sets were calculated within the BG region to search for recurrent mismatch regions over the time period.

3.3 Estimation of Freshwater Release from Sea Ice Melting

The volume of freshwater (V_{fw}) released into the ocean from sea ice melting within a given region can be estimated by:

$$V_{fw} = \sum_{i=1}^{N} \alpha_i a_i h_i \frac{\rho_{ice}}{\rho_{fw}}, \tag{2}$$

where N refers to the number of grid cells inside the region, α represents the grid-cell SIC/100, a_i is the grid-cell area, and h is the melted sea ice thickness. For the sea ice density, ρ_{ice}, and freshwater density, ρ_{fw}, we took the values of 900 kg m^{-3} (Timco & Frederking, 1996) and 1000 kg m^{-3} (Tanaka et al., 2001), respectively. We calculated the September budget of V_{fw} released over the BG region. To achieve this, we defined September 1 as the starting point and the day of maximum sea ice retreat as the endpoint. Subsequently, we compared and quantified the contribution of September's sea ice melting to the in situ FWC reported by Proshutinsky et al. (2019).

3.4 Localization and Characterization of Meltwater Lenses

We analyzed the formation of MWLs every September during our study period (2011-2019), because the ocean surface in the BG has the lowest sea ice cover in September. As sea surface freshening would be expected after sea ice melting, we computed the number of days that each grid cell was covered by sea ice, considering OSISAF SIC $> 10\%$ as a threshold. Using the number of iced days in each grid cell, we were able to identify potential areas influenced by sea ice melting. For each grid cell to be considered as part of a MWL, we applied two criteria: 1) the number of days covered by sea ice (SIC $> 10\%$) must range between 2 to 29 days, i.e. during September at least two days have been ice

covered; and 2) monthly mean values of SSS must be less or equal than 25 psu to ensure the presence of sea-ice meltwaters (Supply et al., 2022). Once the MWLs were delimited, we calculated their area, seawater properties, and the volume of freshwater released from sea ice melting (see Section 3.3). We also evaluated the SSS-SST properties of two large MWLs detected in September 2011 and 2016, as well as the daily SSS and density evolution over a MWL-crossing transect with constant latitude. We analyzed the wind stress and sea ice velocity patterns to search for drivers on the sea surface freshening during sea ice melting and sea surface salinification when sea ice forms.

3.5 Freezing temperature of Seawater

As MWLs form as a result of sea ice melting, it is anticipated that the SST within MWLs might closely approximate the freezing point, particularly during the initial stages of sea ice melting. The freezing temperature of seawater can be conceptually represented as a linear function influenced by both salinity and pressure (Holland & Jenkins, 1999):

$$T_f = \beta S + \kappa + \lambda P, \tag{3}$$

where $\beta = -5.73 \times 10^{-2}$ °C/psu and $\lambda = -7.61 \times 10^{-2}$ °C/MPa are the proportionality constants for salinity (S) and pressure (P), and $\kappa = 8.32 \times 10^{-2}$ °C is the intercept. For this computation, and given the small variability range in comparison with the other two variables, we assumed the standard atmospheric pressure of 0.1 MPa at the SL.

4 Results and Discussion

4.1 Sea Ice Area and Sea Surface Salinity Relationship

The SIA north of 65°N (Fig. 2a) is annually cyclic, reaching its maximum extent in March and its minimum in September, with a decreasing trend of -6.2×10^3 km^2 yr^{-1} during the study period. In our estimations, maxima SIA varies from ~ 8.5 to 9.5×10^6 km^2, and minima varies from ~ 3 to 4×10^6 km^2. Since our study area is confined to latitudes above 65°N, substantial portions of the ocean susceptible to winter sea ice coverage -including the Okhotsk and Bering seas, the Gulf of Alaska, Hudson Bay, and the Labrador Sea- are not included in our estimations. Consequently, our maximum SIA estimates fall below those reported for the entire Northern Hemisphere (Lavergne et al., 2023). However, our minimum estimates align well with the reported SIA index (Lavergne et al., 2023), as sea ice coverage during summer is restricted to very high latitudes. The record low SIA, occurring in 2012 has been recently attributed to a La Niña-driven sea surface warming of the Arctic Pacific sector (Jeong et al., 2022) and is coincident with the anomalously warm stagnant air that contributed to the record-high melt over the Greenland Ice Sheet (GrIS) in 2012 (Nghiem et al., 2012). The monthly average SSS within the observable Arctic region (Fig. 2a) shows a strong synchrony and an identical annual cycle with the sea ice cover. Monthly means of horizontally-averaged SSS vary from ∼31 psu in September, marking the conclusion of the melt season, to ∼35 psu in March, coinciding with peak sea ice coverage. As observed for SIA, the record-low SSS recorded during the study period, approximately 30 psu, took place in September 2012, likely attributable to the increased freshwater released from sea ice and GrIS melting (Tedesco et al., 2013). The saltiest September occurred in 2013, with SSS of around 32 psu, aligning with the highest SIA observed in September throughout the study period. The SSS time series show a negligible decreasing trend of -0.003 psu yr^{-1}. While the observable ocean for SMOS SSS retrieval fluctuates in tandem with sea ice cover, both SIA and SSS exhibit a strong correlation (Fig. 2b). A possible explanation of such a good fitting between both variables ($R^2 = 0.96$) is that the observed sea surface is smaller and southern when sea ice cover expands, leaving only the saltier surface waters of the Norwegian and Barents Seas to be measurable from SMOS. On the other hand, a larger ocean surface is measurable when sea ice retreats, and the fresher SSS retrieved could reveal the

potential capability of SMOS in detecting the sea ice melt footprint, as it has been recently reported in Supply et al. (2022).

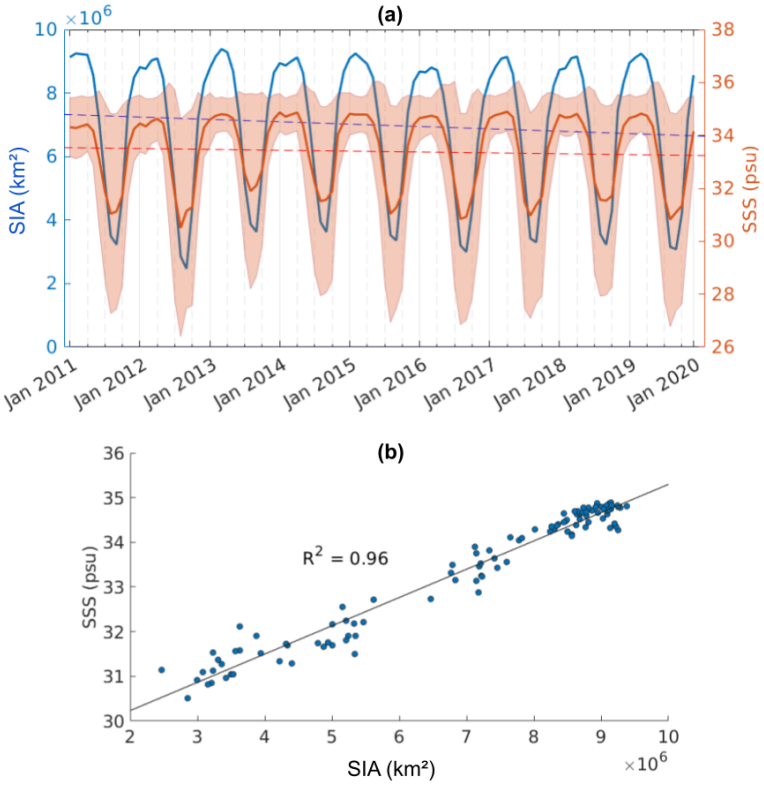

Figure 2: a) Time series of Arctic (>65°N) monthly means of sea ice area (solid blue line) and sea surface salinity (solid orange line). The shadow area shows the standard deviation of SSS and the dashed lines are the linear trends of SIA (blue) and SSS (orange) over the study period. b) Correlation between sea ice cover and SSS.

The SSS and SIA time evolution at the BG scale is shown in Fig. 3. As described above for the Arctic, SIA in the BG also follows a seasonal pattern, accounting for around a tenth of the Arctic SIA. The BG is entirely covered by sea ice (SIA around 9×10^5 km^2) from November to May throughout the entire study period, leading to data gaps in SMOS SSS. Minimum SIA takes place in September and ranges from less than 10^5 km^2 in 2012 to approximately $5.5{\times}10^5$ km^2 in 2013. Monthly means of SSS from June to October do not exhibit a clear pattern, varying from 23 to 29 psu. Relative to 2011, the annual mean SIA values have retreated around 1% in the BG and 0.7% in the Arctic up to 2019. The lowest SIA record of 2012 is contributing to flattening the decreasing trend observed in both the Arctic and the BG from 2011 to 2019 (Figs. 2a and 3a). Regarding the SSS trends, having 2012 as the freshest SSS year at the beginning of the time series may attenuate the observed decline in Arctic SSS and enhance the upward trend in the BG SSS. Moreover, the positive trends observed in the BG for the SSS are also contributing to relax the slope of the SSS negative trend observed in the Arctic.

Examining the SSS-SIA relationship in the BG (Fig. 3b), we observe that, in general, a decreasing trend in SIA ($-0.8{\times}10^3$ km^2 yr^{-1}) does not result in fresher sea surface waters; instead, it leads to a salinification trend of 0.01 psu yr^{-1} (Fig. 3a). Hence, it seems that the sea ice retreat in the BG may not necessarily be accompanied by sea surface freshening. Nonetheless, we suspect that the sea surface conditions in the BG,

observable by SMOS SSS from June to October, experience distinct regimes depending on the phase of the melting season. We propose that during the early stages of the melt season (June-July), sea ice melting induces sea surface freshening, while sea ice formation results in sea surface salinification in the late season (September-October)(see Fig. S1). However, in the middle of the melt season, a transient period is expected, where SIA and SSS may not be tightly synchronized due to other processes (apart from sea ice melting/formation) exerting a more significant influence on sea surface properties. As described in Section 1, the BG is a dynamically complex region, with sea ice distribution highly dependent on atmospheric forcing (Asplin et al., 2009; Petty et al., 2016; Wang, Wekerle, Danilov, Koldunov, et al., 2018) and sea surface properties subjected to inflow rates of Pacific waters through the Bering Strait (Hu et al., 2019; Timmermans & Toole, 2023), which in turn vary periodically with ENSO (Jeong et al., 2022). These and other factors, such as cloud cover, rain/snow fall, riverine inflows, ocean mesoscale eddies, upwellings, or brine rejection might play a non-negligible role on the sea surface properties and the sea ice distribution in the BG (Timmermans & Toole, 2023). Moreover, different free-of-ice regions of the BG become observable each year, likely resulting in capturing different water masses (e.g. from sea ice melting, the Alaskan Coastal Waters or the Mackenzie River influence).

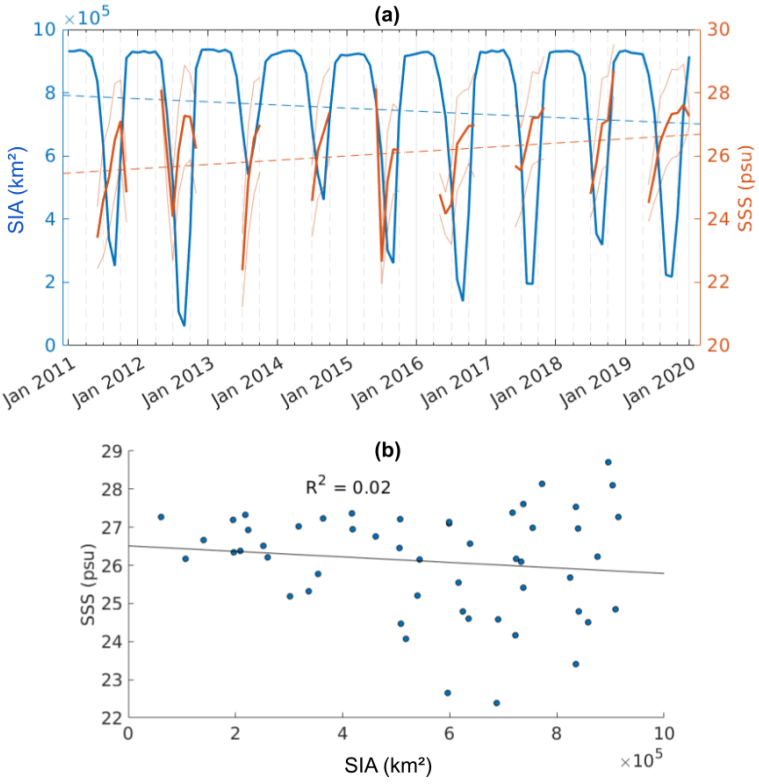

Figure 3: a) Time series of BG's monthly means of sea ice area (solid blue line) and sea surface salinity (solid orange line). The light orange lines shows the standard deviation of SSS and the dashed lines are the linear trends of SIA (blue) and SSS (orange) over the study period. b) Correlation between SIA and SSS in the BG.

4.2 Reanalysis Performance vs. Remote Observations in the BG

Model reanalysis outputs can serve to fill the spatial and temporal gaps in remote observations, extending their applicability even to ocean properties beneath the ice. They are very useful to get a more comprehensive picture of the sea ice-SSS relationship. September is the month with the lowest sea ice cover in the BG region (Fig. 3a), so a larger number of satellite SSS observations can be retrieved. Therefore, for all Septembers from 2011 to 2019, we first compare the SSS retrieved from SMOS against that solved by two model reanalysis: TOPAZ4b, which assimilates SMOS SSS data (Xie et al., 2023), and ORAS5, which has been reported as the best SSS performer in the BG (Hall et al., 2021).

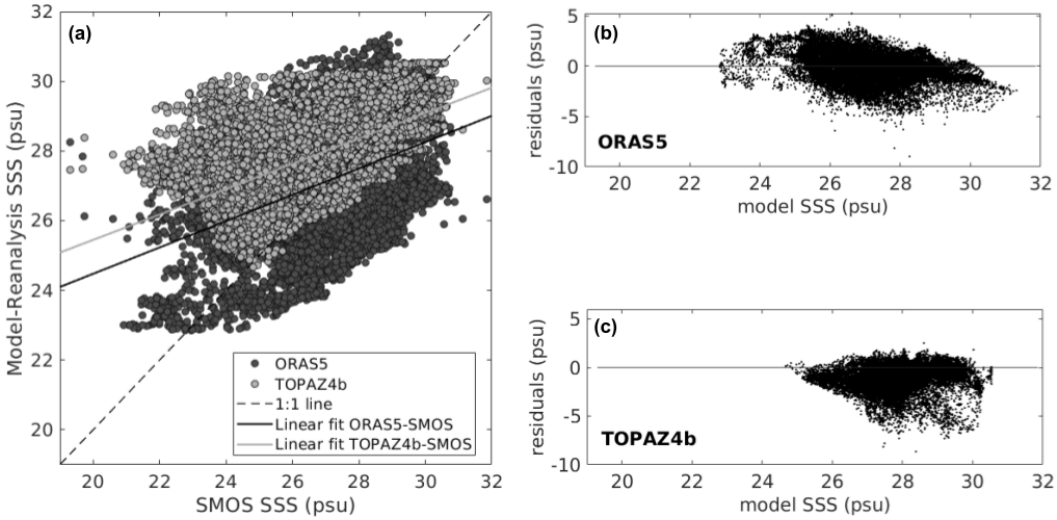

Figure 4: a) Co-located observed (SMOS) versus modeled (ORAS5 and TOPAZ4b) monthly means of SSS. b) and c) SSS residuals (SMOS-Model) against modeled ORAS5 and TOPAZ4b SSS, respectively. To get the correct view of the model performance, the x-axis limits in b) and c) are those of SMOS-observed SSS.

Both ORAS5 and TOPAZ4b models exhibit significant deviations from observed SMOS SSS, failing to capture the freshest waters detected by the satellite (monthly mean SSS of 19.3 psu) (Fig. 4a). The correlation slopes for observed-modeled SSS are approximately 0.37 in both models, with intercepts of 16 and 18 psu, and R^2 values of 0.2 and 0.4 for ORAS5 and TOPAZ4b, respectively, indicating a poor agreement between observed and modeled SSS. The difference in the correlation coefficient between the two models is attributed to the distribution of their outputs. Specifically, ORAS5 displays a wide range of residuals (Fig. 4b), ranging from +5 to -9 psu, with mean SSS of 27.1 $\pm$1.3 psu, and values spanning 22.8 to 31.3 psu. In contrast, TOPAZ4b (Fig. 4c) exhibits a more restricted range of positive residuals (approximately +2 psu) and a similar range for negative values. However, TOPAZ4b provides mean SSS of 28.0 $\pm$0.9 psu, and values ranging from 24.7 to 30.5 psu, which show larger constrictions in the freshest waters compared to ORAS5. When comparing minimum salinity, ORAS5 (TOPAZ4b) reaches approximately 23 (25) psu, while SMOS measures near 19 psu. However, these minima are not synchronized. Notably, the most significant discrepancies between SMOS and modeled SSS, reaching up to -9 psu (Fig. 4b, c), precisely align with SMOS recording the minimum salinity, while the models indicate $\sim$ 28 psu (see Fig. 4a).

The September surface distribution of SSS and its residuals (SMOS-Model) is shown in Fig. 5. For a more comprehensive analysis and to identify sea ice as a potential source

of freshwater inducing SMOS-Model mismatch, the number of days each pixel has been covered by sea ice is also included in Fig. 5a. Our results suggest a negative bias (model being saltier than observations) close to the coast in the two models (see also Fig. S2), as also shown in Hall et al. (2021). The fresher areas detected by SMOS SSS offshore are likely induced by the Mackenzie River plume (Juul-Pedersen et al., 2008; Pickart, 2004; Doxaran et al., 2015; Nghiem et al., 2014), as previously reported for the Yukon River's offshore waters (Vazquez-Cuervo et al., 2021). Considering that the SSS residuals' distribution is masked by SMOS data (Fig. 5b), the absence of data (blanked regions in the northern and isolated areas) indicates that the ocean is covered by sea ice (see Fig. 5a). Thus, looking at Fig. 5c, negative bias are also found close to some ice edges and around small iced areas. Previous studies have documented enhancements in ocean salinity predictions with the incorporation of SMOS SSS assimilation into TOPAZ4b (Xie et al., 2023). Nevertheless, our findings suggest that the assimilation process falls short in accurately capturing the freshest SSS, as depicted in Figs. 4 and 5c. Despite being previously identified as the best performer in comparison to in situ SSS observations (Hall et al., 2021), our comparative analysis reveals that ORAS5 neither aligns with SMOS SSS in the freshest areas (Fig. S2). The challenge of aligning model solutions with observations at the sea surface arises from the fact that the sea surface serves as a boundary within ocean models' domains. Furthermore, since other variables, such as SST or SL, must be solved by the model in close proximity to the sea surface boundary, imposing a weak tolerance in SSS assimilation may result in divergences between model-derived and observed SSS values.

In summary, for all Septembers from 2011 to 2019 (see Fig. S3), SMOS SSS detects fresher patches of sea surface waters in two main areas: near the sea-ice edge, where sea ice was present for a limited number of days (monthly SSS of about 19 to 25 psu), and the influence area of the Mackenzie River discharge (monthly SSS around 26 psu). Analyzing the SMOS SSS distribution in the BG and whether a given grid cell was covered by sea ice that eventually melted (see Fig. 5, and Movie S1 as an example), our results suggest that models poorly represent river and sea-ice-melt waters, whereas SMOS demonstrates accurate representation. This is particularly noteworthy given the impact of the model limitations on estimating the FWC in the BG, which lead to its underestimation (Umbert et al., 2023).

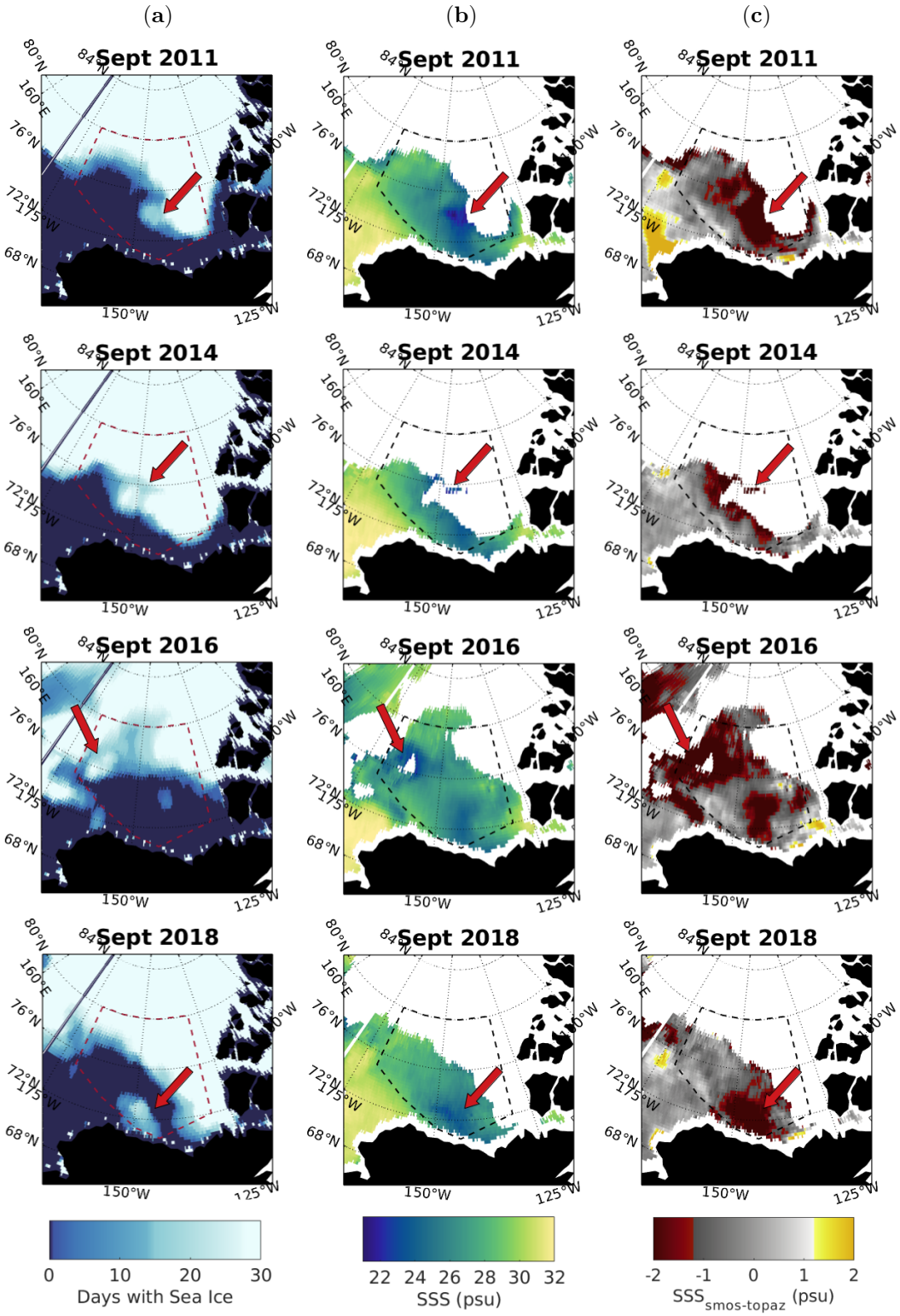

Figure 5: Spatial distribution of a) number of days covered by sea ice (SIC > 10%), b) SMOS SSS and c) SSS residuals: observed (SMOS) minus modeled SSS (TOPAZ4b). Dashed line delimits the Beaufort Gyre region. The colorbar in c) has been truncated (see full range of values in Fig. 4). The red arrows point the locations where SMOS SSS retrieves information of sea ice meltwaters.

4.3 Estimations of Sea Ice Meltwater in the BG

Sea ice meltwater constitutes a significant component of the FWC in the BG. Utilizing Eqns. 1 and 2, we computed the melted SIA and the corresponding V_{fw} released into the ocean for all Septembers. Our findings reveal interannual fluctuations in both the extent and thickness of melted sea ice, consequently leading to variations in the released V_{fw}, ranging from 0 to ∼120 km^3 (Fig. 6). Minimum records are given in 2013, 2012 and 2017. The minima observed in 2012 align with high Arctic temperatures in the preceding autumn-winter (2011-2012), impeding the formation and thickening of sea ice (Overland et al., 2017; Perovich et al., 2017). Moreover, the sustained high atmospheric temperatures in early spring of 2012 (Jeong et al., 2022) led to an earlier onset of sea ice melting compared to a typical year, resulting in a reduced sea ice cover to be melted at the beginning of September 2012 (see Movie S2 in Supp. Information). The 2013 minimum, however, is attributed to a distinct cause: an Arctic cold event. This cold event resulted in a September characterized by a sea ice freshwater budget of 0 km^3, indicating no melting but sea ice formation (Movie S3). In 2014, increased SST anomalies in the North Pacific triggered a stage of Arctic warming (Overland et al., 2018). This warming, in turn, facilitated melting of such extensive and thick sea ice inherited from 2013. This phenomenon is reflected in our results as the most significant release of sea-ice meltwater in 2014 (Fig. 6c).

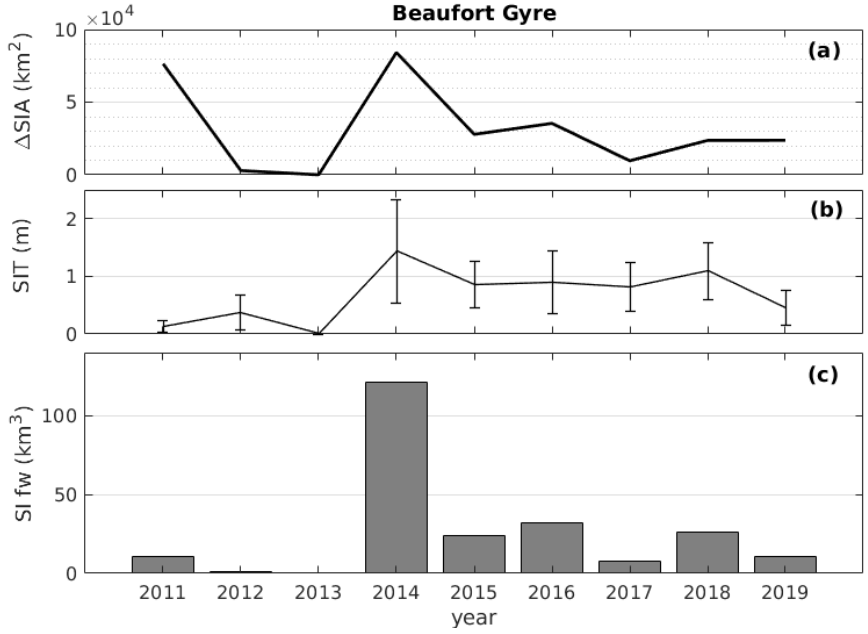

Figure 6: September sea ice budget from 2011 to 2019 in the Beaufort Gyre: a) melted sea-ice area, b) mean sea ice thickness within the melted sea-ice area, and c) freshwater volume released from sea ice melting (Eqn. 2).

Our estimations indicate that the V_{fw} released into the ocean from sea ice melting during September in the BG could contribute up to ∼30% of the average annual rate of freshwater accumulation in the BG (Proshutinsky et al., 2019). However, this sea ice meltwater is partially incorporated in the water column, partially advected out of the region by wind-driven ocean currents, and partially susceptible to be refrozen. Recent model simulations suggest that sea ice serves as a minor freshwater source of the FW accumulation in the BG (Wang et al., 2019). Thus, while we cannot definitively deter-

mine the net contribution of September's sea ice meltwater to either the total or the accumulation rate of FWC in the BG, we can analyze its distribution at the sea surface using SMOS SSS.

4.4 Monitoring Meltwater Lenses using SMOS SSS from 2011 to 2019

We exploit the SMOS capability to detect MWLs from sea ice melting (Supply et al., 2022) along with OSTIA SST and ORAS5 wind stress to investigate about mixing drivers and residence time of sea-ice meltwaters at the sea surface. MWLs have been defined following the methods in 3.4 and are shown in Fig. 7 contoured in cyan. The extent and distribution of MWLs exhibit inter annual variability. In 2012, 2017, and 2019, the MWLs are notably scarce in number and extent, whereas the most substantial MWLs are identified in 2011, 2015, and 2016. MWLs are usually found attached or close to the ice edge, except for September 2018, when an isolated MWL is found at the southernmost location of the BG.

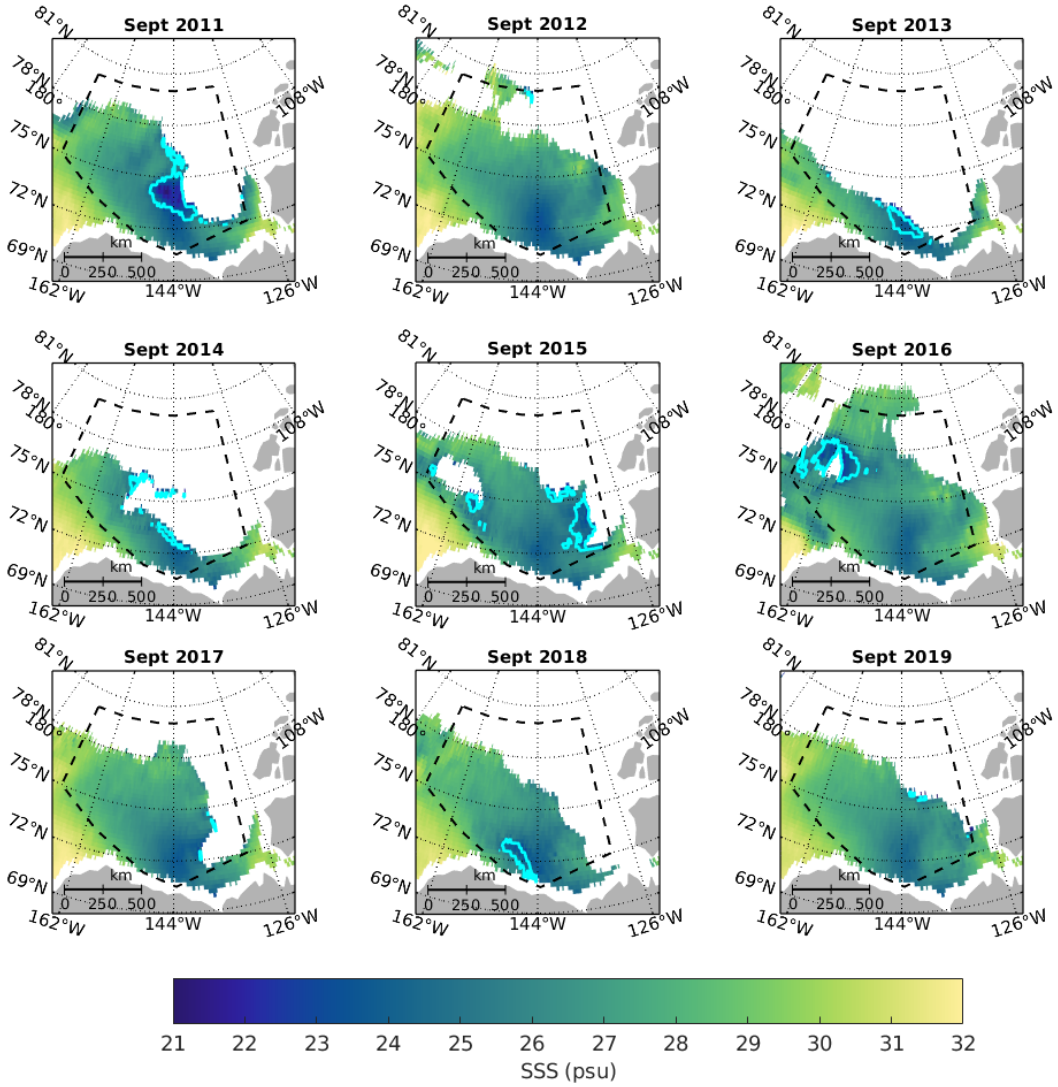

Figure 7: Location of the meltwater lenses (contoured in cyan) over September means of SMOS SSS from 2011 to 2019. The dashed black line delimits the BG region.

Some MWLs' properties are shown in Fig. 8. These properties include: SSS, area, SIT and the V_{fw} released from SI melting. Horizontal monthly means of SSS inside the MWLs are quite stable at ∼24 psu, with minimum and maximum grid-cell values ranging from 16 psu (in 2011) to 27 psu (in 2015), respectively (Fig. 8a). Given the methods used to locate the MWLs (Section 3.4), the primary source of freshwater would be the sea ice melting. The larger the meltwater lens, the wider the range of SSS variability (Fig. 8a, b), likely reflecting increased mixing with surrounding waters at the lens edges.

The total area covered by these MWLs also shows large variability during the study period (Fig. 8b). The MWL area shows minima values of $< 10^4$ km^2 in 2012 and 2017, aligning with those minima observed in the BG (Fig. 6). However, the largest meltwater lenses, with an area of > 6 x 10^4 km^2, take place in 2011 and 2015, which differs from the years of the largest sea ice extent in the BG. Horizontally averaged monthly means of SIT ranges from 0.1 to 1 m, with most of the years being ≤ 0.5 m (Fig. 6c). The V_fw released from sea ice melting (Section 3.3) within the meltwater lenses varies from ∼0.1 km^3 to ∼3 km^3 (Fig. 8d), which represents up to 10% of the estimations for the BG (Fig. 6c). The years of maximum meltwater release are 2011, 2016, and 2014, coincident with either larger MWL areas, thicker SI, or both.

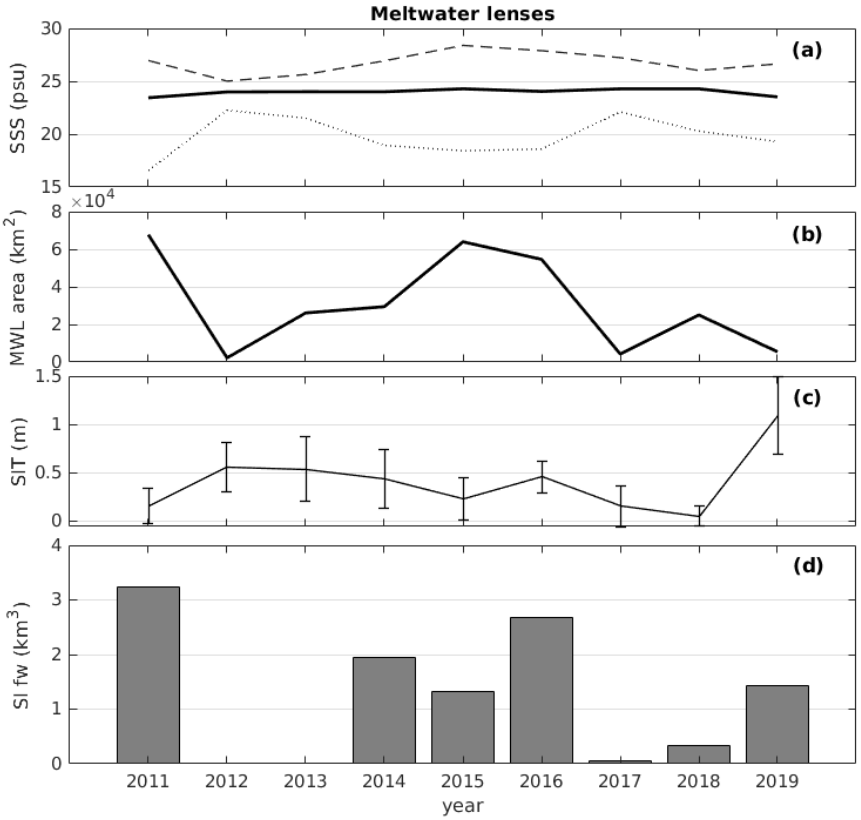

Figure 8: Characteristics of the meltwater lenses detected by SMOS in every September from 2011 to 2019: a) mean (solid dark line), minimum (dotted gray line) and maximum (dashed gray line) sea surface salinity; b) area; c) mean ORAS5 sea ice thickness (± 1 Std bars); and d) Freshwater volume released from sea ice melting.

4.5 Studying Large Meltwater Lenses Detected in 2011 and 2016

The high area/perimeter ratio of the 2011 and 2016 MWLs makes them particularly suitable for studying the temporal evolution of hydrographic properties. This is because they experience lower mixing with surrounding sea waters compared to those with a low area/perimeter ratio, increasing the likelihood of retaining imprints from sea-ice meltwater.

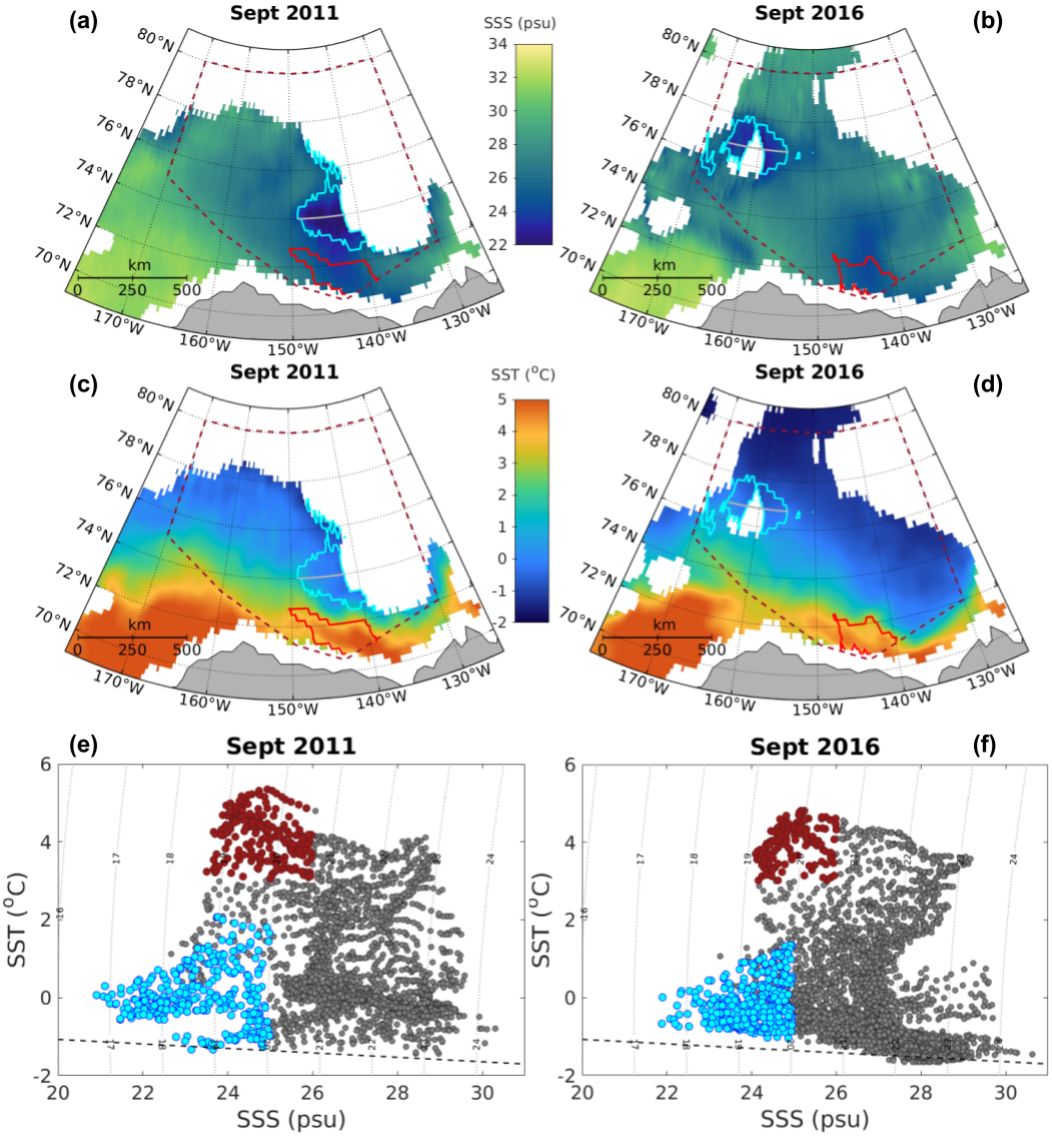

Figure 9: September monthly means of a, b) SMOS sea surface salinity; and c, d) OSTIA sea surface temperature in the BG, during September 2011. Dashed red polygon delimits the BG region, solid cyan line is the MWL perimeter, solid gray line indicates the transect used in Fig. 10, and solid red line delimits the river-influence area. e, f) Monthly SST vs SSS properties within the BG (gray dots), inside the MWL (light blue dots), and within the river-influence area (red dots). Dashed line indicates the freezing temperature for any given salinity according to Eqn. (3). Panels to the left (right) refer to 2011 (2016).

In Fig. 9 the hydrographic properties of large MWLs detected in 2011 and 2016 are shown. In September 2011, the MWL was localized in the southeast quadrant of the BG, while in September 2016, it was situated in the northwest quadrant (contoured in cyan in Fig. 9a-d). The freshest waters inside the MWLs (Fig. 9a, b) take lower SSS values than those observed in the whole BG region, with horizontally-averaged monthly mean SSS ranging from 21 to 25 psu. A different fresh patch (24 to 26 psu) south of the BG is detected (contoured in red), between 145°W and 150°W (contoured in red), which, due to the temperate SST of 3 to 5 ºC (Fig. 9c, d), can be attributed to the influence of the Mackenzie River (Doxaran et al., 2015). In the SST-SSS diagram (Fig. 9e, f) the differentiation of these two water masses (sea-ice meltwater and riverine waters) becomes clear, with the lowest salinity and near-freezing SST properties corresponding to the MWL's water mass and the low salinity but relatively warm properties corresponding to the riverine waters (Nghiem et al., 2014). Looking at the SST-SSS diagram along with the SST spatial distribution (Fig. 9e, f and 9c, d), we see that the lowest and near-freezing temperatures of the sea surface waters in the BG are those spreading along the entire sea ice margin. Nonetheless, looking at the SSS distribution (Fig. 9a, b), we observe water salinification on large areas of the sea ice margin, so we can ensure that those sea-ice marginal waters have undergone some mixing, which is not reflected in SST. Therefore, SSS seems to be a better option than SST when trying to localize MWLs and analyze the time evolution of mixing/dilution processes of the meltwaters released from sea ice melting).

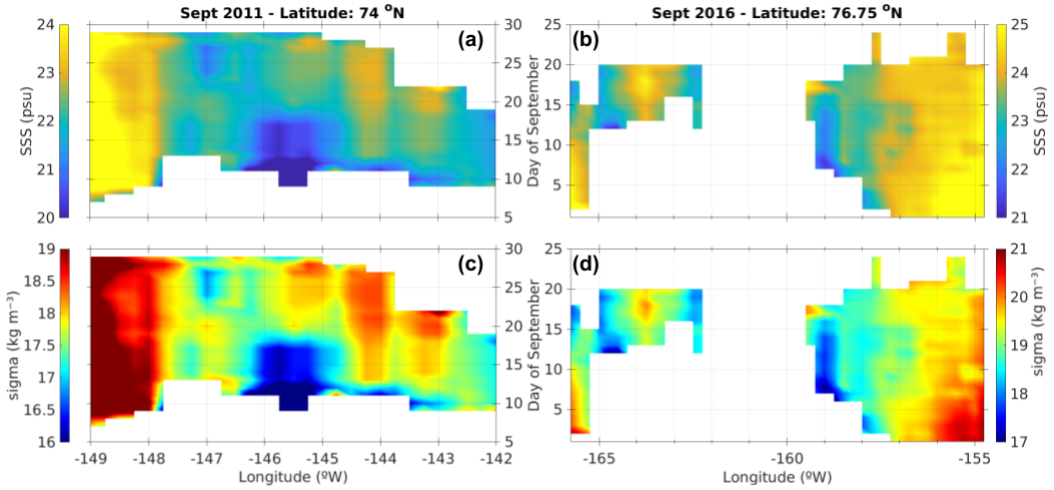

Figure 10: September Hovmöller diagrams of sea surface properties along transects of constant latitude inside the MWLs (see transects in Fig. 9): a, b) salinity from SMOS, and c, d) sigma calculated from SMOS SSS and OSTIA SST. Panels to the left (right) refer to 2011 (2016). Note that the colorbar limits differ between years and blanked areas indicate sea ice presence.

The daily evolution of sea surface salinity and sigma (i.e. $\rho_{sw}-1000$ kg m^{-3}) within the MWL during September of 2011 and 2016 are shown in Fig. 10. It is noteworthy the strong correlation between density and salinity, denoting the minimal influence of temperature on density within these cold waters. The plots reveal different characteristics between both years. Concerning sea surface freshening, the imprint of sea ice melting in September 2011 (see Fig. 10a, b) manifested a conspicuous presence, characterized by a substantial expanse of comparatively fresh and low-density water (SSS ~21 psu and sigma ~16.5 kg/m^3). This expanse persisted at the core of the meltwater lens for a duration of up to 10 days. This prolonged presence of low-mixing conditions within this region is indicative of the convergent regime associated with anticyclonic atmospheric

forcing (refer to Fig. 11a, c). Conversely, in the year 2016 (Fig. 10c, d), a significant sea ice mass continually occupied the central region of the meltwater lens throughout September. The influence of sea ice meltwater was comparatively marginal, likely linked to the divergent dynamics resulting from cyclonic wind forcing (refer to Fig. 11b, d). The most extensive and freshest sector was located in the central-eastern portion (approximately 159°W). This sector persisted for a period of up to one week, which, due to the prevailing southwest wind forcing and the constant presence of sea ice in close proximity, can be attributed to a sustained source of sea ice meltwaters. Additionally, an area of fresh water was observed near 165°W, emerging on September 12, after the sea ice melting. This area of freshwater persisted until the formation of sea ice (water refreezing) on September 20, likely denoting low-mixing conditions during that week.

Concerning the saltier areas, in September 2011, the majority of the saltiest and densest waters within the MWL (SSS ∼24 psu and sigma ∼19 kg m^{-3}), occupied the westernmost region of the MWL (Fig. 10a, b). This area was the farthest and isolated from the sea ice pack influence, being in permanent contact with surrounding (saltier and warmer) waters. In the easternmost sector, specifically at 143, 144 and 145ºW, elevated salinity and density (SSS ∼24 psu and sigma ∼19 kg m^{-3}) were detected one to two weeks before sea ice formation. Such signal of increased salinity and density became even stronger on the day before sea ice formation. Given the prevailing northeast winds in that area (see Fig. 11a), it could be anticipated that some of the saltier waters, generated following brine rejection, might have been advected southwestward from the ice pack vicinity. Although denser and saltier water typically tends to sink, the influence of wind stress could counteract this tendency by inducing upwelling. This phenomenon also has implications for our understanding of brine rejection as detected by SMOS. Since Martínez et al. (2022) showed that sea ice presence might induce lower SSS values, our observations lead us to conclude that the observed increase in SSS is not a consequence of sea ice contamination but rather originates from saline water sources. In 2016, the easternmost region of the MWL predominantly contained the densest and saltiest waters, characterized by SSS ∼25 psu and sigma ∼21 kg m^{-3}. Notably, a localized surge in salinity and density was recorded at around 159.5°W on September 17, just before the onset of sea ice formation. As described above for 2011, this observed salinity increase could potentially be associated with brine rejection. However, validation through in situ measurements or high-resolution model outputs would be necessary to confirm this hypothesis.

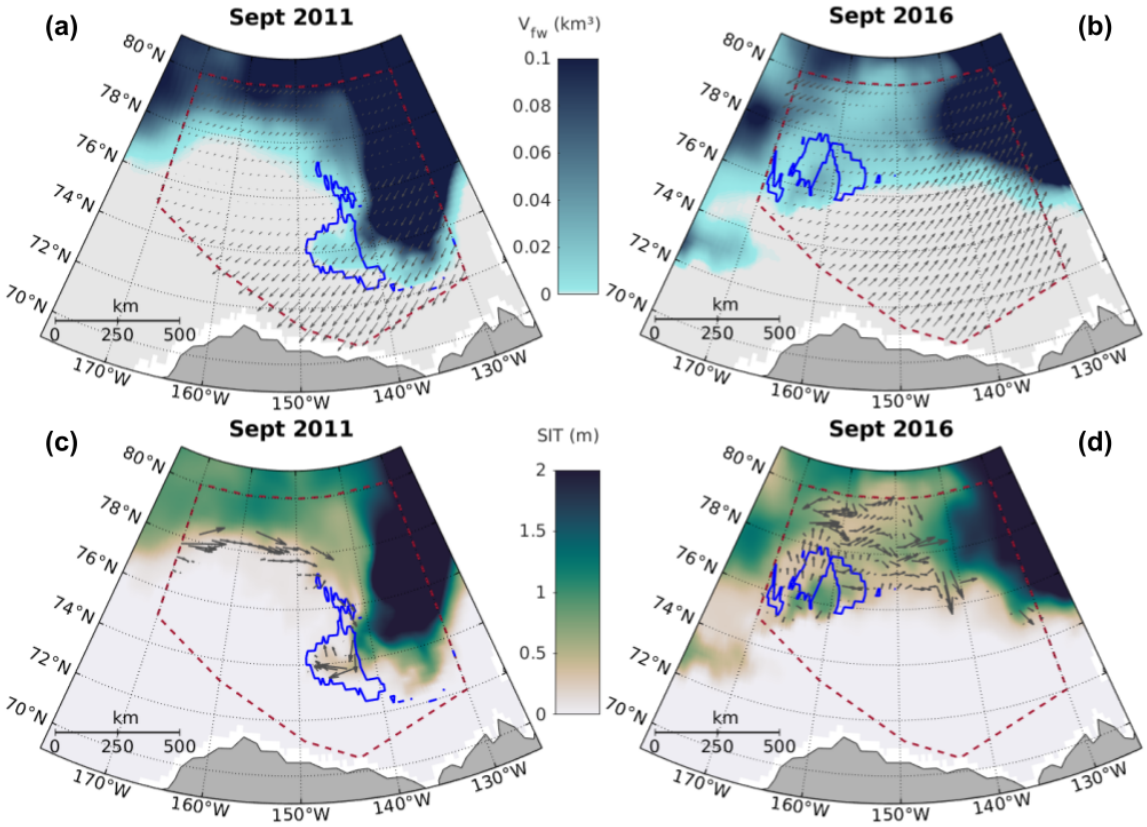

Figure 11: a, b) September monthly mean volume of solid freshwater at each grid cell and superimposed vectors of monthly wind stress. c, d) September monthly means of sea ice thickness, with sea ice velocity vectors on top of it. Dashed red polygon delimits the BG region and solid blue line is the MWL perimeter. Panels to the left (right) refer to 2011 (2016).

The monthly predominant wind maps over the BG reveal different patterns in September 2011 and 2016 (Fig. 11a, b). September 2011 was characterized by an anticyclonic regime associated with the high-pressure system over the BG, as reported in previous studies (Serreze & Barrett, 2011; Timmermans & Marshall, 2020). Ice velocity maps in September 2011 (Fig. 11c) show that a detached ice floe from the main pack experienced convergent dynamics during the first half of the month, leading to the accumulation of meltwater within the center of the MWL, with relatively low mixing, which was detected by SMOS SSS. In contrast, during September 2016, dominant winds exhibited a cyclonic pattern over the BG (Fig. 11b), resulting in a divergent sea ice movement within the MWL (Fig. 11d). In Movie S4 of the *Sup. Info*, we can observe how at the beginning of September 2016, sea ice coverage was minimal, decreasing slightly until reaching the minimum on September 5. Following that day, SIA started to rise in the northwest quadrant of the BG. We speculate that the cyclonic wind pattern introduced cold north winds, potentially promoting sea ice growth over the northwest quadrant of the BG (Fig. 11b). Consequently, despite observing a larger area of ice-free ocean in September 2016 compared to September 2011, both the melted SIA and the $V_f w$ were smaller in September 2016 than in 2011 (Fig. 6a, c).

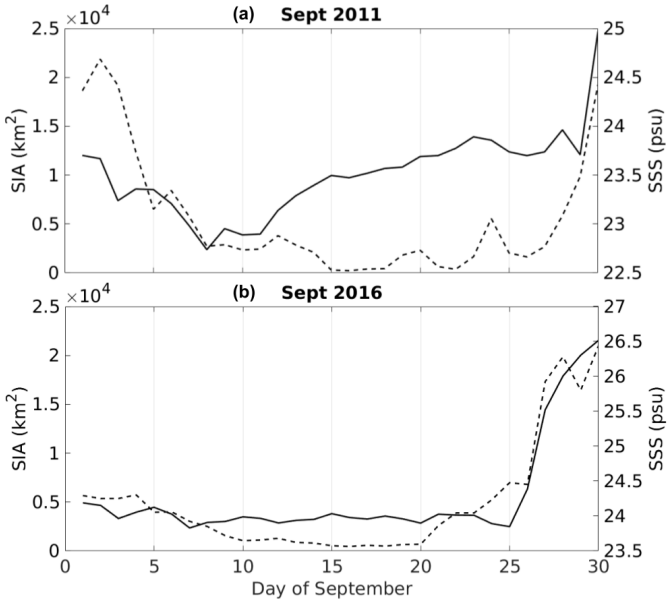

Figure 12: Daily evolution of sea ice area (SIA, dashed line) and mean sea surface salinity (SSS, solid line) inside the MWLs in a) 2011 and b) 2016 (see Figs. 9 and 11 to see the MWL region).

The daily evolution of SIA and SSS within the MWL is shown in Fig. 12. At the beginning of September 2011, SIA exceeded 2 x 10^4 km^2, and the average SSS was approximately 23.7 psu. The minimum salinity (∼22.7 psu) occurred around September 7, while the minimum SIA (0 km^2 kilometers) was on September 16. Both variables reached their maximum at the end of the month, with SSS around 25 psu and SIA approximately 2 x 10^4 km^2. In September 2016, a piece of sea ice at the center of the MWL remained unmelted, failing to strictly meet the criteria for inclusion in the MWL (refer to Section 3.4), therefore it was excluded from the SIA calculation. The behavior of SIA and SSS during September 2016 was similar to that of 2011 but with different values: less ice and higher salinity overall. At the beginning of the month, SSS was around 24.2 psu, and SIA was 0.5 x 10^4 km^2, with both variables starting to increase during the last third of the month, reaching approximately 26.5 psu and 2 x 10^4 km^2, respectively.

To conclude our investigation, we return to the analysis of the SSS-SIA relationship at a local scale within the MWLs (Fig. 12). Our results reveal close synchrony in the daily evolution of both variables throughout September in the two years. If sea ice melts, the ocean surface reduces its salinity (this occurs roughly in the first ten days of September). Conversely, if sea ice grows, the ocean surface becomes saltier (see Fig. 12 during the last third of the month). During the second third of the month, there is a transient state where the correlation in the daily evolution of SSS and SIA is not as tight. During this transient state, when the ice-free area is at its maximum, water mixing induced by winds or local circulation is more likely to have a pronounced impact on the ocean surface, leading to increases in salinity. Additionally, the momentum associated to this phenomena may temporarily inhibit sea ice formation (Roquet et al., 2022). There seems to be a time lag between the response of the two variables: SSS appears to be more reactive, while SIA requires a longer response time. Additionally, hysteresis associated with phase changes in water could slow down the ice formation response compared to SSS changes. This idea of a transient state is consistent with the outcomes presented in Section 4.1. We can extend this concept to the BG by regarding it as a large MWL. In

this scenario, September could be viewed as the third period, corresponding to the sea ice formation stage. Consequently, both SIA and SSS are expected to increase and exhibit a positive correlation, aligning with our expectations and illustrated in Fig. S1.

5 Conclusions

In our temporal analysis spanning 2011 to 2019, utilizing OSISAF SIC and SMOS SSS data, we discovered a close synchronization and positive correlation between SIA and SSS at both large (Arctic region) and local (MWL) scales. However, on the regional scale of the BG, the temporal evolution of SIA and SSS diverged, likely due to prolonged ice coverage, and leading to significant space-time gaps in SSS data. The ice-free period is restricted to July to October, during which a complex interplay influenced by various freshwater sources occurs. SSS outputs from reanalysis models, namely ORAS5 and TOPAZ4b, were compared with SMOS SSS observations every September, revealing significant discrepancies. Notably, these models failed to accurately depict the freshening effects observed in SSS after sea ice melting, a phenomenon effectively captured by SMOS SSS. Our results suggest that sea ice melting in September may contribute up to 30% to the reported annual mean FWC accumulation within the Beaufort Gyre. Therefore, the model's inaccuracy could contribute to the previously reported mismatch between observational and model-based FWC estimations.

Exploiting the SMOS SSS capabilities on detecting sea surface freshening from sea ice melting, we identified MWL locations within the BG during September from 2011 to 2019. MWLs exhibited annual variability, with notable scarcity in 2012, 2017, and 2019, contrasting with substantial presence in 2011, 2015, and 2016. These MWLs presented the freshest SSS within the BG, along with lower SST compared to areas influenced by the Mackenzie River plume. Daily SSS variations within MWLs not only indicated that SMOS SSS captures sea-ice meltwater but also suggested that it may capture events of brine rejection after sea ice formation. This discovery opens avenues for further studies and the continuous monitoring of sea-ice-ocean interactions using SMOS SSS.

Wind patterns emerged as pivotal in mixing sea ice meltwater with surrounding waters and accumulating it at the surface through wind-driven convergent circulation. On a local scale within MWLs, the temporal evolution of SSS and SIA demonstrated a strong correlation during both stages of sea ice melting and sea ice formation. Transitional periods with reduced correlation were observed during the transition from sea ice melting to formation when ice-free area in the ocean is present, suggesting that drivers of water mixing might play a significant role in the SSS changes.

In summary, this research highlights the useful capabilities of SMOS SSS data in helping to unravel the intricate dynamics of sea ice melting, freshwater input, and sea surface salinity in the Arctic, which is especially valuable in the context of a changing climate.

Open Research Section

All data used in this study are freely available through different repositories. SMOS SSS data are freely distributed from the Barcelona Expert Center `https://doi.org/10.20350/digitalCSIC/12620`. SIC data were obtained from OSI-450 and OSI-430b products at `https://doi.org/10.15770/EUM_SAF_OSI_0008` and `https://doi.org/10.15770/EUM_SAF_OSI_NRT_2008`, respectively. Data set of OSTIA SST was downloaded through `https://doi.org/10.48670/moi-00165`. ORAS5 and TOPAZ 4b reanalysis data on SSS, SIT, wind stress and sea ice velocity ca be downloaded from `https://doi.org/10.24381/cds.67e8eeb7` and `https://doi.org/10.48670/moi-00007`, respectively.

Acknowledgments

E. De Andrés is supported by Margarita-Salas Grant No. UP2021-035 under the Next Generation-EU program. M. Umbert is funded by Marie Skłodowska-Curie Grant Agreement No. 840374. This study was also financed by the MCIN/AEI projects DINGLAC (PID2020-113051RB-C31) and ARCTIC-MON (PID2021-125324OB-I00), and from the ESA Arctic+Salinity project (AO/1-9158/18/I-BG). This work represents a contribution to the CSIC Thematic Interdisciplinary Platform PTI-POLARCSIC, and is supported by the Spanish Government through the "Severo Ochoa Centre of Excellence" accreditation (CEX2019-000928-S).

References

Armitage, T. W. K., Manucharyan, G. E., Petty, A. A., Kwok, R., & Thompson, A. F. (2020). Enhanced eddy activity in the Beaufort Gyre in response to sea ice loss. *Nature communications*, *11*(1), 1–8.

Asplin, M. G., Lukovich, J. V., & Barber, D. G. (2009). Atmospheric forcing of the Beaufort Sea ice gyre: Surface pressure climatology and sea ice motion. *Journal of Geophysical Research*, *114*(4), C00A06. doi: 10.1029/2008JC005127

Belkin, I. M., Levitus, S., Antonov, J., & Malmberg, S.-A. (1998). "Great Salinity Anomalies" in the North Atlantic. *Progress in Oceanography*, *41*(1), 1–68. doi: 10.1016/S0079-6611(98)00015-9

Brodzik, M. J., Billingsley, B., Haran, T., Raup, B., & Savoie, M. H. (2012). EASE-Grid 2.0: Incremental but Significant Improvements for Earth-Gridded Data Sets. *ISPRS International Journal of Geo-Information*, *1*(1), 32–45. doi: 10.3390/ijgi1010032

Carmack, E. C., Yamamoto-Kawai, M., Haine, T. W. N., Bacon, S., Bluhm, B. A., Lique, C., ... Others (2016). Freshwater and its role in the Arctic Marine System: Sources, disposition, storage, export, and physical and biogeochemical consequences in the Arctic and global oceans. *Journal of Geophysical Research: Biogeosciences*, *121*(3), 675–717.

Cornish, S. B., Muilwijk, M., Scott, J. R., Marson, J. M., Myers, P. G., Zhang, W., ... Marshall, J. (2023). Impact of sea ice transport on Beaufort Gyre liquid freshwater content. *Climate Dynamics*, *61*(3-4), 1139–1155. doi: 10.1007/s00382-022-06615-4

Dickson, R. R., Meincke, J., Malmberg, S.-A., & Lee, A. J. (1988, jan). The "great salinity anomaly" in the Northern North Atlantic 1968–1982. *Progress in Oceanography*, *20*(2), 103–151. doi: 10.1016/0079-6611(88)90049-3

Doxaran, D., Devred, E., & Babin, M. (2015). A 50 particles delivered by the Mackenzie River into the Beaufort Sea (Canadian Arctic Ocean) over the last 10 years. *Biogeosciences*, *12*(11), 3551–3565. doi: 10.5194/bg-12-3551-2015

EUMETSAT Ocean and Sea Ice Satellite Application Facility, Darmstadt, Germany. (2017). *Global sea ice concentration climate data record 1979-2015 (v2.0, 2017), [Online]. Norwegian and Danish Meteorological Institutes.* doi: 10.15770/EUM_SAF_OSI_0008

EUMETSAT Ocean and Sea Ice Satellite Application Facility, Darmstadt, Germany. (2019). *Global sea ice concentration interim climate data record 2016 onwards (v2.0, 2019), [Online]. Norwegian and Danish Meteorological Institutes.*

Fournier, S., Lee, T., Tang, W., Steele, M., & Olmedo, E. (2019). Evaluation and intercomparison of SMOS, Aquarius, and SMAP sea surface salinity products in the Arctic Ocean. *Remote Sensing*, *11*(24), 3043.

Fournier, S., Lee, T., Wang, X., Armitage, T. W. K., Wang, O., Fukumori, I., & Kwok, R. (2020). Sea Surface Salinity as a Proxy for Arctic Ocean Freshwater Changes. *Journal of Geophysical Research: Oceans*, *125*(7). doi: 10.1029/2020JC016110

Giles, K. A., Laxon, S. W., Ridout, A. L., Wingham, D. J., & Bacon, S. (2012).

Western Arctic Ocean freshwater storage increased by wind-driven spin-up of the Beaufort Gyre. *Nature Geoscience*, *5*(3), 194–197. doi: 10.1038/ngeo1379

Good, S., Fiedler, E., Mao, C., Martin, M. J., Maycock, A., Reid, R., ... Worsfold, M. (2020). The Current Configuration of the OSTIA System for Operational Production of Foundation Sea Surface Temperature and Ice Concentration Analyses. *Remote Sensing*, *12*(4), 720. doi: 10.3390/rs12040720

Greene, C. A., Thirumalai, K., Kearney, K. A., Delgado, J. M., Schwanghart, W., Wolfenbarger, N. S., ... Blankenship, D. D. (2019). The Climate Data Toolbox for MATLAB. *Geochemistry, Geophysics, Geosystems*, *20*(7), 3774–3781. doi: 10.1029/2019GC008392

Haine, T. W. N., Curry, B., Gerdes, R., Hansen, E., Karcher, M., Lee, C., ... Others (2015). Arctic freshwater export: Status, mechanisms, and prospects. *Global and Planetary Change*, *125*, 13–35.

Haine, T. W. N., Siddiqui, A. H., & Jiang, W. (2023). Arctic freshwater impact on the Atlantic Meridional Overturning Circulation: status and prospects. *Philosophical Transactions of the Royal Society A: Mathematical, Physical and Engineering Sciences*, *381*(2262). doi: 10.1098/rsta.2022.0185

Hall, S. B., Subrahmanyam, B., & Morison, J. H. (2021). Intercomparison of Salinity Products in the Beaufort Gyre and Arctic Ocean. *Remote Sensing*, *14*(1), 71. doi: 10.3390/rs14010071

Holland, D. M., & Jenkins, A. (1999). Modeling Thermodynamic Ice–Ocean Interactions at the Base of an Ice Shelf. *Journal of Physical Oceanography*, *29*(8), 1787–1800. doi: 10.1175/1520-0485(1999)029⟨1787:MTIOIA⟩2.0.CO;2

Holliday, N. P., Bersch, M., Berx, B., Chafik, L., Cunningham, S., Florindo-López, C., ... Others (2020). Ocean circulation causes the largest freshening event for 120 years in eastern subpolar North Atlantic. *Nature communications*, *11*(1), 585.

Hu, X., Myers, P. G., & Lu, Y. (2019). Pacific Water Pathway in the Arctic Ocean and Beaufort Gyre in Two Simulations With Different Horizontal Resolutions. *Journal of Geophysical Research: Oceans*, *124*(8), 6414–6432. doi: 10.1029/2019JC015111

Jahn, A., & Holland, M. M. (2013). Implications of Arctic sea ice changes for North Atlantic deep convection and the meridional overturning circulation in CCSM4-CMIP5 simulations. *Geophysical Research Letters*, *40*(6), 1206–1211. doi: 10.1002/grl.50183

Jahn, A., & Laiho, R. (2020). Forced Changes in the Arctic Freshwater Budget Emerge in the Early 21st Century. *Geophysical Research Letters*, *47*(15), 1–10. doi: 10.1029/2020GL088854

Jeong, H., Park, H., Stuecker, M. F., & Yeh, S. (2022). Record Low Arctic Sea Ice Extent in 2012 Linked to Two-Year La Niña-Driven Sea Surface Temperature Pattern. *Geophysical Research Letters*, *49*(9), 1–11. doi: 10.1029/2022GL098385

Johnson, H. L., Cornish, S. B., Kostov, Y., Beer, E., & Lique, C. (2018). Arctic Ocean Freshwater Content and Its Decadal Memory of Sea-Level Pressure. *Geophysical Research Letters*, *45*(10), 4991–5001. doi: 10.1029/2017GL076870

Juul-Pedersen, T., Michel, C., & Gosselin, M. (2008). Influence of the Mackenzie River plume on the sinking export of particulate material on the shelf. *Journal of Marine Systems*, *74*(3-4), 810–824. doi: 10.1016/j.jmarsys.2008.02.001

Kilic, L., Prigent, C., Aires, F., Boutin, J., Heygster, G., Tonboe, R. T., ... Donlon, C. (2018). Expected performances of the Copernicus Imaging Microwave Radiometer (CIMR) for an all-weather and high spatial resolution estimation of ocean and sea ice parameters. *Journal of Geophysical Research: Oceans*, *123*(10), 7564–7580.

Krishfield, R. A., Proshutinsky, A., Tateyama, K., Williams, W. J., Carmack, E. C.,

McLaughlin, F. A., & Timmermans, M. (2014). Deterioration of perennial sea ice in the Beaufort Gyre from 2003 to 2012 and its impact on the oceanic freshwater cycle. *Journal of Geophysical Research: Oceans*, *119*(2), 1271–1305. doi: 10.1002/2013JC008999

Lavergne, T., Aaboe, S., Neuville, A., Sørensen, A., & Eastwood, S. (2023). *Product User Manual for the Sea Ice Index, version 2.2* (Tech. Rep.). EUMETSAT.

Lavergne, T., Sørensen, A. M., Kern, S., Tonboe, R., Notz, D., Aaboe, S., ... Pedersen, L. T. (2019). Version 2 of the EUMETSAT OSI SAF and ESA CCI sea-ice concentration climate data records. *The Cryosphere*, *13*(1), 49–78. doi: 10.5194/tc-13-49-2019

Martínez, J., Gabarró, C., Turiel, A., González-Gambau, V., Umbert, M., Hoareau, N., ... Fernández, D. (2022). Improved BEC SMOS Arctic Sea Surface Salinity product v3.1. *Earth System Science Data*, *14*(1), 307–323. doi: 10.5194/essd-14-307-2022

Nghiem, S. V., Hall, D. K., Mote, T. L., Tedesco, M., Albert, M. R., Keegan, K., ... Neumann, G. (2012, oct). The extreme melt across the Greenland ice sheet in 2012. *Geophysical Research Letters*, *39*(20), 6–11. doi: 10.1029/2012GL053611

Nghiem, S. V., Hall, D. K., Rigor, I. G., Li, P., & Neumann, G. (2014). Effects of Mackenzie River discharge and bathymetry on sea ice in the Beaufort Sea. *Geophysical Research Letters*, *41*(3), 873–879.

Overland, J. E., Hanna, E., Hanssen-Bauer, I., Kim, S. J., Walsh, J. E., Wang, M., ... Thoman, R. L. (2017). *Surface Air Temperature [in Arctic Report Card 2017]* (Tech. Rep.). National Oceanic and Atmospheric Administration.

Overland, J. E., Wang, M., & Ballinger, T. J. (2018). Recent increased warming of the Alaskan marine Arctic due to midlatitude linkages. *Advances in Atmospheric Sciences*, *35*(1), 75–84. doi: 10.1007/s00376-017-7026-1

Perovich, D., Meier, W., Tschudi, M., Farrell, S., Hendricks, S., Gerland, S., ... Webster, M. (2017). *Sea Ice [in Arctic Report Card 2017]* (Tech. Rep.). National Oceanic and Atmospheric Administration.

Petty, A. A., Hutchings, J. K., Richter-Menge, J. A., & Tschudi, M. A. (2016). Sea ice circulation around the Beaufort Gyre: The changing role of wind forcing and the sea ice state. *Journal of Geophysical Research: Oceans*, *121*(5), 3278–3296. doi: 10.1002/2015JC010903

Pickart, R. S. (2004). Shelfbreak circulation in the Alaskan Beaufort Sea: Mean structure and variability. *Journal of Geophysical Research*, *109*(C4), C04024. doi: 10.1029/2003JC001912

Polyakov, I. V., Pnyushkov, A. V., Alkire, M. B., Ashik, I. M., Baumann, T. M., Carmack, E. C., ... Yulin, A. (2017). Greater role for Atlantic inflows on sea-ice loss in the Eurasian Basin of the Arctic Ocean. *Science*, *356*(6335), 285–291. doi: 10.1126/science.aai8204

Proshutinsky, A., Bourke, R. H., & McLaughlin, F. A. (2002). The role of the Beaufort Gyre in Arctic climate variability: Seasonal to decadal climate scales. *Geophysical Research Letters*, *29*(23), 11–15.

Proshutinsky, A., Krishfield, R., Timmermans, M.-L., Toole, J., Carmack, E., McLaughlin, F., ... Shimada, K. (2009). Beaufort Gyre freshwater reservoir: State and variability from observations. *Journal of Geophysical Research: Oceans*, *114*(C1).

Proshutinsky, A., Krishfield, R., Toole, J. M., Timmermans, M., Williams, W., Zimmermann, S., ... Zhao, J. (2019). Analysis of the Beaufort Gyre Freshwater Content in 2003–2018. *Journal of Geophysical Research: Oceans*, *124*(12), 9658–9689. doi: 10.1029/2019JC015281

Rabe, B., Karcher, M., Schauer, U., Toole, J. M., Krishfield, R. A., Pisarev, S., ... Kikuchi, T. (2011). An assessment of Arctic Ocean freshwater content changes from the 1990s to the 2006–2008 period. *Deep Sea Research Part I: Oceano-*

graphic Research Papers, *58*(2), 173–185. doi: 10.1016/j.dsr.2010.12.002

Rahmstorf, S., Box, J. E., Feulner, G., Mann, M. E., Robinson, A., Rutherford, S., & Schaffernicht, E. J. (2015). Exceptional twentieth-century slowdown in Atlantic Ocean overturning circulation. *Nature Climate Change*, *5*(5), 475–480. doi: 10.1038/nclimate2554

Rantanen, M., Karpechko, A. Y., Lipponen, A., Nordling, K., Hyvärinen, O., Ruosteenoja, K., ... Laaksonen, A. (2022). The Arctic has warmed nearly four times faster than the globe since 1979. *Communications Earth Environment*, *3*(1), 168. doi: 10.1038/s43247-022-00498-3

Roquet, F., Ferreira, D., Caneill, R., Schlesinger, D., & Madec, G. (2022). Unique thermal expansion properties of water key to the formation of sea ice on Earth. *Science Advances*, *8*(46), 1–10. doi: 10.1126/sciadv.abq0793

Serreze, M. C., & Barrett, A. P. (2011). Characteristics of the Beaufort Sea High. *Journal of Climate*, *24*(1), 159–182. doi: 10.1175/2010JCLI3636.1

Shimada, K., Carmack, E. C., Hatakeyama, K., & Takizawa, T. (2001). Varieties of shallow temperature maximum waters in the Western Canadian Basin of the Arctic Ocean. *Geophysical Research Letters*, *28*(18), 3441–3444. doi: 10.1029/2001GL013168

Shimada, K., Itoh, M., Nishino, S., McLaughlin, F., Carmack, E., & Proshutinsky, A. (2005). Halocline structure in the Canada Basin of the Arctic Ocean. *Geophysical Research Letters*, *32*(3), 1–5. doi: 10.1029/2004GL021358

Solomon, A., Heuzé, C., Rabe, B., Bacon, S., Bertino, L., Heimbach, P., ... Tang, H. (2021). Freshwater in the Arctic Ocean 2010–2019. *Ocean Science*, *17*(4), 1081–1102. doi: 10.5194/os-17-1081-2021

Supply, A., Boutin, J., Kolodziejczyk, N., Reverdin, G., Lique, C., Vergely, J., & Perrot, X. (2022). Meltwater Lenses Over the Chukchi and the Beaufort Seas During Summer 2019: From In Situ to Synoptic View. *Journal of Geophysical Research: Oceans*, *127*(12), 1–17. doi: 10.1029/2021JC018388

Tanaka, M., Girard, G., Davis, R., Peuto, A., & Bignell, N. (2001, aug). Recommended table for the density of water between 0 C and 40 C based on recent experimental reports. *Metrologia*, *38*(4), 301–309. doi: 10.1088/0026-1394/38/4/3

Tedesco, M., Fettweis, X., Mote, T., Wahr, J., Alexander, P., Box, J. E., & Wouters, B. (2013). Evidence and analysis of 2012 Greenland records from spaceborne observations, a regional climate model and reanalysis data. *The Cryosphere*, *7*(2), 615–630. doi: 10.5194/tc-7-615-2013

Timco, G., & Frederking, R. (1996). A review of sea ice density. *Cold Regions Science and Technology*, *24*(1), 1–6. doi: 10.1016/0165-232X(95)00007-X

Timmermans, M.-L., & Marshall, J. (2020). Understanding Arctic Ocean Circulation: A Review of Ocean Dynamics in a Changing Climate. *Journal of Geophysical Research: Oceans*, *125*(4). doi: 10.1029/2018JC014378

Timmermans, M.-L., & Toole, J. M. (2023). The Arctic Ocean's Beaufort Gyre. *Annual Review of Marine Science*, *15*(1), 223–248. doi: 10.1146/annurev-marine-032122-012034

Umbert, M., Andrés, E. D., Sánchez, M., Gabarró, C., González-gambau, V., García, A., ... Catany, R. (2023). Contribution of satellite sea surface salinity to the estimation of liquid freshwater content in the Beaufort Sea. *Ocean Science*, *preprint*. doi: 10.5194/egusphere-2023-1510

Umbert, M., Gabarro, C., Olmedo, E., Gonçalves-Araujo, R., Guimbard, S., & Martinez, J. (2021). Using Remotely Sensed Sea Surface Salinity and Colored Detrital Matter to Characterize Freshened Surface Layers in the Kara and Laptev Seas during the Ice-Free Season. *Remote Sensing*, *13*(19), 3828.

Vazquez-Cuervo, J., Gentemann, C., Tang, W., Carroll, D., Zhang, H., Menemenlis, D., ... Steele, M. (2021). Using Saildrones to Validate Arctic Sea-Surface Salinity from the SMAP Satellite and from Ocean Models. *Remote Sensing*,

13(5), 831. doi: 10.3390/rs13050831

Wang, Q., Wekerle, C., Danilov, S., Koldunov, N., Sidorenko, D., Sein, D., ... Jung, T. (2018). Arctic Sea Ice Decline Significantly Contributed to the Unprecedented Liquid Freshwater Accumulation in the Beaufort Gyre of the Arctic Ocean. *Geophysical Research Letters*, *45*(10), 4956–4964. doi: 10.1029/2018GL077901

Wang, Q., Wekerle, C., Danilov, S., Sidorenko, D., Koldunov, N., Sein, D., ... Jung, T. (2019). Recent Sea Ice Decline Did Not Significantly Increase the Total Liquid Freshwater Content of the Arctic Ocean. *Journal of Climate*, *32*(1), 15–32. doi: 10.1175/JCLI-D-18-0237.1

Wang, Q., Wekerle, C., Danilov, S., Wang, X., & Jung, T. (2018). A 4.5 km resolution Arctic Ocean simulation with the global multi-resolution model FESOM 1.4. *Geoscientific Model Development*, *11*(4), 1229–1255.

Xie, J., Raj, R. P., Bertino, L., Mart´, J., Gabarró, C., & Catany, R. (2023). Assimilation of sea surface salinities from SMOS in an Arctic coupled ocean and sea ice reanalysis. *Ocean Science*, *19*(2), 269–287.

Yang, Q., Dixon, T. H., Myers, P. G., Bonin, J., Chambers, D., van den Broeke, M. R., ... Mortensen, J. (2016). Recent increases in Arctic freshwater flux affects Labrador Sea convection and Atlantic overturning circulation. *Nature Communications*, *7*(1), 10525. doi: 10.1038/ncomms10525

Zhang, J., Lindsay, R., Steele, M., & Schweiger, A. (2008). What drove the dramatic retreat of arctic sea ice during summer 2007? *Geophysical Research Letters*, *35*(11), 1–5. doi: 10.1029/2008GL034005

Zhang, J., Steele, M., & Woodgate, R. (2008). The role of Pacific water in the dramatic retreat of arctic sea ice during summer 2007. *Chinese Journal of Polar Science*, *19*(2), 93–107.

Zhang, J., Weijer, W., Steele, M., Cheng, W., Verma, T., & Veneziani, M. (2021). Labrador Sea freshening linked to Beaufort Gyre freshwater release. *Nature communications*, *12*(1), 1–8.